Modeling and simulation of a stand-alone wind turbine supplying an inductive load through a long cable

Zakaria Al-Omari[1], Walid Emar[2]
[1]Department of Renewable Energy Engineering, Faculty of Engineering, Isra University, Amman, Jordan
[2]Department of Electrical Engineering, Faculty of Engineering, Isra University, Amman, Jordan

Article Info	ABSTRACT
	This paper considers the principles of modeling, control, and simulation of variable speed wind turbines (VSWTs), based on a stand-alone doubly fed induction generator (DFIG). The DFIG is used to feed a three-phase highly inductive load through a long cable via a three-phase multi-level frequency converter (MLFC). The proposed MLFC increases the number of voltage levels with less power electronic components as compared to the conventional back-to-back AC/DC/AC converter. The length of the cable (transmission line TL) influences a mismatch between the load and TL impedances; therefore, a reflected signal will occur. If the "incident signal" is a "continuous AC waveform", these waveforms will mix with another oncoming "incident waveform", creating stationery waveforms called "standing waves". The simulation process shows that the value of the transient's over-voltage that appears either on the windings of the DFIG or across the load reaches twice the DC-link voltage periodically, which may cause premature failure of the DFIG windings and cable insulations. Usually, this is produced by generating high harmonics within the loads. Therefore, the main benefit of using the MLFC is the significant reduction of the total harmonic distortion and enhancement of the load voltage waveforms. This was verified, primarily by using the "MATLAB/Simulink, Simplorer 7" simulation software.

Corresponding Author:

Zakaria Al-Omari
Renewable Energy Engineering Department, Faculty of Engineering, Isra University
Amman, 11622, Jordan
Email: zakaria.alomari@iu.edu.jo

1. INTRODUCTION

Recently, as wind power has become a green and sustainable power, its dissemination in the power system (PS) has increased significantly and is expected to rise in the future [1]-[4]. The growing integration of wind turbines (WTs) raised the interest in studying the impact of integrated wind units on the static and dynamic performance of the PS. This impact of WTs integration is not generic and can be positive or negative depending on the wind generating system type and load profile [2].

The small WTs operating with a stand-alone doubly fed induction generator (DFIG) and RL load are expected to grow steadily in the coming years. There is no specific definition of small-scale WTs. This paper assumes the capacity of small WTs to be from about 1 kW to 100 kW, with a generation voltage level of less than 1kV [5]. The speed at which WTs operate is usually fixed or variable, although the variable-speed operation is preferred. The main advantage of a system operating at a fixed speed is the ability to connect it to the grid directly without the need for additional control and power electronic processors or converters. Variable-speed wind turbines VSWT systems can generate more electrical energy from a large wind speed (WS) range system while reducing the pressure in the driving system. The efficiency of the electrical energy

produced can also be improved by using special power electronic techniques to control the speed of these turbines [6]. The DFIG-based wind PS consists, of a controlled IG fed by energy from both sides, from the rotor and stator circuits, and a power electronics frequency converter with a DC-link, in addition to the excitation system and a VSWT.

In this paper, the VSWT equipped with a stand-alone DFIG feeding an isolated RL load through a long cable is studied. The IG is excited by the fixed capacitor at the stator terminals, but the rotor terminals are connected to the RL load via a MLFC to maintain a constant voltage at the DC-link and load, simultaneously. Additionally, this paper covers the influence of cable length on system performance. It is well known that by increasing the length of the cable, its impedance will increase. Such an increment will influence the mismatch between the load impedance and characteristic impedance of the cable. In its turn, the mismatching will create voltage-current drips and reflection waves that resonate with the whole system at frequencies determined by the cable's length and propagation speed constant. These reflection waves (standing waves) are studied through simulation only. The simulation results showed that using pulse width modulation PWM multi-level frequency converter MLFC can prevent the destruction of the load and insulation of the cable, compared to conventional frequency converters. It is difficult, to design and simulate a unified control model for the whole VSWT system, which effectively reflects the performance characteristics of a such complicated system [7]. Therefore, this paper mainly focuses on the modeling of such a complicated system.

The MLFC system discussed in this article is a three-phase, three-level voltage source inverter connected to a rectifier with a DC-link in between. This MLFC provides an alternative to the traditional converter to decrease (or even avoid) the quantities of series-connected semiconductor switches. In the three-level MLFC, each switching unit must withstand the half value of the DC-link voltage. Therefore, the three-level MLFC can ensure a three-phase voltage source with a lesser degree of distortion harmonics compared to the analogous two-level frequency converter [8]-[10].

Since the load is highly inductive with also large capacitances of the cables, fluxes could be generated by both windings of the generator, stator, and rotor windings. Therefore, if the generator is running at nearly synchronous speed, the rotor voltage is minimal, and the torque developed by the generator may be very high due to the induction-ness of the system. However, if the rotor voltage is adjusted to be nearly equal to that of the stator circuit, then the IG torque would be very small. On the other side, the control of the IG torque could also allow the control of the generator power [11], [12].

The output power of the WT depends strongly on the rotational speed of the turbine, the WS, and the pitch angle of the inclination of the blades in a non-linear manner. Therefore, the control unit is designed to adjust the speed and the turbine torque accordingly. Therefore, this paper is focused on the modeling and simulation of the IG torque using the MLFC control system. In addition to the behavior of the output power, the control of the DC-link voltage using PI regulators and a chopper circuit is also discussed. These control processes are independently treated as their control circuits are technically and physically separated [12]-[14].

2. VARIABLE SPEED WT SYSTEMS

The primary application of wind turbines is to convert wind energy to electrical energy. The extraction power is given by (1).

$$P = \frac{1}{2}\rho A V^3 \tag{1}$$

Where, A is the swept area, [m^2]; V is the wind speed, [m/s]; and ρ is the air density, [kg / m^3]. The (1) describes the total power that can be extracted from a WT, which is limited to maximum theoretical efficiency. This limitation in power quantity is based on Betz's law stating that the maximum performance factor or the power coefficient of the wind turbine C_P of a WT is 59.3%. By defining the input and output variables of a WT, expressions of the relationships between the input and output variables can be easily obtained. Therefore, the principle of operation of a WT can be described using the mechanical power extracted from the turbine, as in (2) [15]-[20].

$$P = \frac{1}{2}\rho A V^3 C_P(\lambda, \beta) \tag{2}$$

Where β is the pitch angle of the blade and λ is the tip-speed ratio.

The output torque of the WT model is determined depending on the WS. Hence, the coefficient of power, C_P is a non-linear function of β and λ. This allows the tip-speed ratio to be formulated as in (3).

$$\lambda_{tur} = \frac{r \, \omega_{tur}}{V} \Rightarrow V = \frac{r \, \omega_{tur}}{\lambda_{tur}} \tag{3}$$

Modeling and simulation of a stand-alone wind turbine supplying an inductive ... (Zakaria Al-Omari)

Where ω_{tur} is the optimal turbine angular velocity, [rad/sec] that corresponds to λ_{tur}. Substituting the value of V in (2), then the turbine power is obtained by (4).

$$P_{tur} = \frac{1}{2} \rho A \left(\frac{r \omega_{tur}}{\lambda_{tur}}\right)^3 C_{p(max)} = k \omega_{tur}^3 \tag{4}$$

Dividing in (4) by the WT angular velocity ω_{tur}, then the turbine torque is obtained by (5).

$$T_{tur} = \frac{1}{2} \rho A \left(\frac{r}{\lambda_{tur}}\right)^3 \omega_{tur}^2 C_{p(max)} = k \omega_{tur}^2 \tag{5}$$

Where $k = \frac{1}{2} \rho A \left(\frac{r}{\lambda_{tur}}\right)^3$ is constant. The (4) and (5) indicate that the maximum extractable turbine power is directly proportional to the cubic WS, and the turbine torque is proportional to the square WS [14]-[16]. The (2) shows that the WT power depends on two terms. The former, $\frac{1}{2} \rho A V^3$, is directly proportional to the cube of the WS, while the latter, $C_p(\lambda, \beta)$, is a variable quantity. The first term is unpredictable. However, the second term $C_p(\lambda, \beta)$, can be controlled by changing the values of $\omega/$ and or β. The power coefficient $C_p(\lambda, \beta)$ of the turbine can be obtained by (6).

$$C_p(\lambda, \beta) = \sum_{i,j=1...4} \lambda^i \beta^j \tag{6}$$

The power coefficient $C_P (\lambda, \beta)$ is very important since it provides accurate data on the aerodynamic efficiency of the WTs system. Figure 1 shows the nonlinear relationships between C_P and the tip-speed ratio λ which results in an exponential increase in C_P and reaches its maximum value. After that, the increase in the tip-speed ratio (λ) leads to a decrease in the C_P. Meanwhile, if the output power of WT is less than the nominal value, β is set to be zero for most WT systems.

Hence, increasing β results in a significant decrease in C_P and the WT power capacity, so it is effectively adjusted to reduce the WT output power when it exceeds the nominal value, or it is set to its maximum value, 90° to stop the power generation under high WS conditions. The difference between the fixed-speed WT system and its counterpart of variable speed can be described based on the coefficient of power $C_p(\lambda)$. In the fixed-speed WT system, λ can't be regulated because the speed (ω) is uncontrollable. So that, control of the C_P indeed results in the control of the angular velocity (ω) and pitch angle (β) [9], [14].
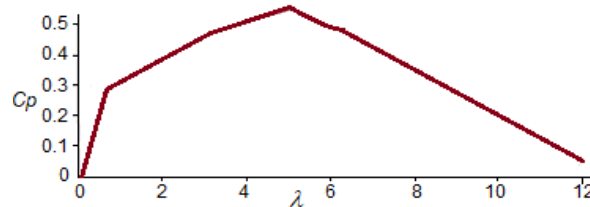

Figure 1. A plot of C_P versus λ

3. POSSIBLE MODEL CONTROL TECHNIQUES FOR A STAND-ALONE DFIG-BASED VSWT WITH AN RL LOAD.

There are two possible circuit configurations that could be used between DFIG and the isolated RL load. The former interfacing circuit connection between them may be implemented using two back-to-back PWM converters connected between the rotor and the load. The later configuration that could be operated effectively for the DFIG with an isolated RL load is to connect the load to the DFIG stator via a three-phase MLFC and a three-phase rectifier [12], [17]-[20]. The former is usually used as an ultimate solution, but it requires additional power devices that increase the cost and complexity of the system. The alternative solution adopted in this paper is the use of a diode-clamped three-level three-phase voltage source inverter installed with three neutral levels [5]. It is known that the same control and modulation circuit described for the DFIG with the two-level back-to-back frequency converter can be applied for the three-level MLFC. The only difference is that the three-level MLFC also needs an equalizing scheme for the DC-voltage power outlet as discussed in [5], [8].

3.1. MLFC model with uncontrolled DC-link voltage power port

Figure 2 shows the control block diagram of a VSWT system. The main goal is to control the IG torque and flux in order to regulate the apparent (active/reactive) power that the MLFC exchanges with the RL load. In this paper, the MLFC, DC side is considered to be connected to the RL load through a three-phase diode rectifier representing an ideal DC voltage source.
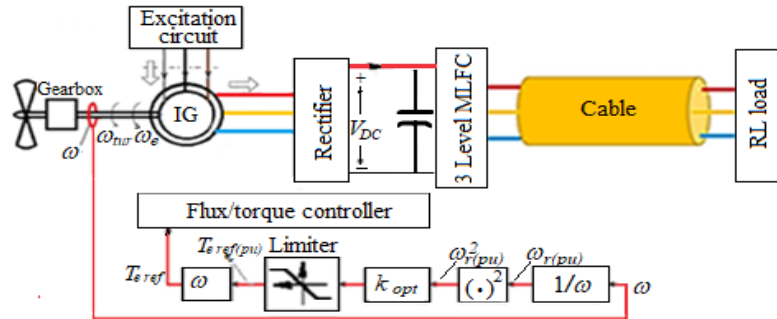

Figure 2. A schematic diagram of the DFIG-based VSWT shows the generator torque-command generator and the uncontrolled DC-link power

As previously discussed, to increase the turbine power capacity, the torque of the system should be controlled in rate to the square of the rotor speed according to (5). This is formulated by means of the torque reference instruction "T_{eref}" shown in Figure 2. Due to the inertia of the wind PS, the rotor speed changes slowly even if the WS is subjected to high fluctuations, and at the same time, the torque response to these changes in speed is very fast. Therefore, the IG torque exactly follows its reference value, and the ideal operating point with the IG's equilibrium condition is tightly and easily reached [5]-[17].

Note, that the induced voltage of the DFIG rotor is maximum when the rotor is blocked, and zero at synchronous speed, n_s. Therefore, the choice of the DC-link voltage value and the generator windings turns ratio should consider the parameters of the IG and the permissible differences in the speed of the rotor.

To ensure the IG is not dangerously overloaded in critical WS conditions, the IG torque known as per-unit torque is determined according to (4) and (5) and based on the implementation of the power optimization strategy. Thus, the wind turbine $P_{tur(pu)}$, and $T_{tur(pu)}$ are obtained by (7) and (8) respectively [16]-[19].

$$P_{m(pu)} = k\omega^3_{m(pu)} \tag{7}$$

$$T_{m(pu)} = k\omega^2_{m(pu)} \tag{8}$$

The MLFC-controlled circuit is shown in Figure 3 according to IG torque requirements, WS fluctuations, and DFIG parameters.

3.2. Modelling of MLFC and the reflected wave process (RWP) of RL load
3.2.1. Long cables "TL" model

Figure 2 illustrates the stand-alone DFIG-based VSWT supplying an isolated three-phase RL load through a long cable and MLFC. The MLFC produces High-frequency PWM voltage with a "rising/falling" period which mostly occurs in the range of [10ns – 100ns] depending on the commutation instrument types, load circumstances, and gate drivers [20].

With a high slew rate (dv/dt), a long cable acts as a TL line even at a short length [20], [21]. Figure 3 shows the RL load model with a lossless TL, where the MLFC is modeled as a PWM voltage source with an impedance Z_S (generally, $Z_S \approx 0$), and the load impedance Z_L. As for the model, the characteristic impedance of the long cable Z_o is obtained by (9).

$$Z_O = \sqrt{\frac{L_O}{C_O}} \tag{9}$$

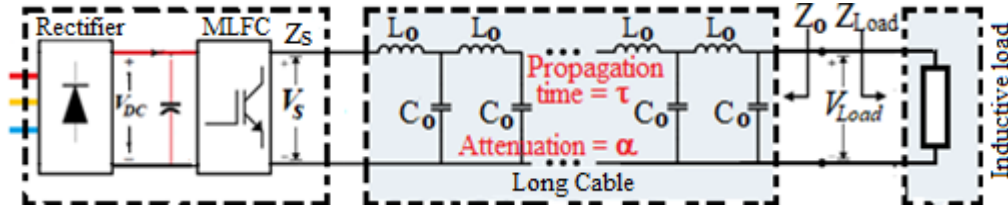Where L_o and C_o are the distributed inductance and capacitance per unit [22].

Figure 3. A common model for the DFIG - based wind PS feeding an RL with a long cable

3.2.2. Fundamentals of the reflected voltage wave (RVW)

In a speed-regulated drive, the PWM voltage pulses generated by the inverter voltage source travel along the cable in the same way as traveling waves travel along power lines, due to the mismatch between the long cable and the load impedances [23]-[25]. The propagation constant of the speed **v** is determined as in (10).

$$v = \frac{1}{\sqrt{L_O \, C_O}} \tag{10}$$

The propagation delay of the long cable τ is obtained by (11) [22].

$$\tau = l\sqrt{L_O \, C_O} \tag{11}$$

The RWP is represented by the bloc scheme demonstrated in Figure 4, where the cable is depicted by a block $\alpha \, e^{-\tau s}$; that is, the incident RVW is detained by a time constant τ when moving between the MLFC and load is attenuated by a coefficient α depending on the cable L_O and C_O [26]. Referring to Figure 4, $V_{sn}^x(s)$ and $V_{sL}^x(s)$ are the voltages at MLF and the load terminal sides in the frequency domain, where x = (+) or (-); "+ is forward-propagation" whilst "- is backward-propagation", n = 1,2,3 designates the nth propagation cycle.
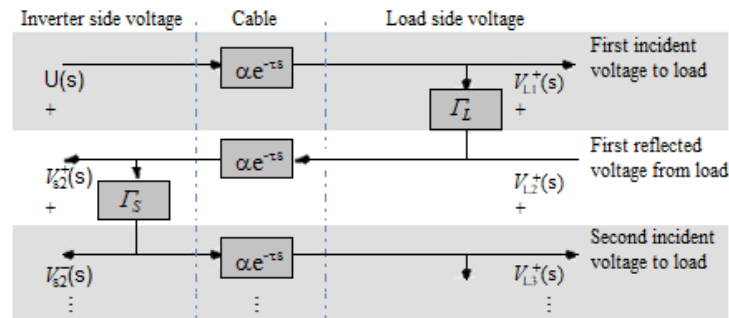

Figure 4. A block-scheme of the RWP

The Laplace transform of the voltage pulse U(s), v_s generated by the MLFC voltage v_s, reaches the load terminals after a time propagation delay τ and then is reflected due to the impedance mismatch between the load and cable. The reflected voltage $V_{L1}^-(s)$ and the incident voltage $V_{L1}^+(s)$ are obtained by (12) and (13).

$$V_{L1}^-(s) = \Gamma_L V_{L1}^+(s) \tag{12}$$

$$V_{L1}^+(s) = U(s)e^{-\tau s} \tag{13}$$

Where Γ_L is the constant of the reflection at the RL load side is obtained by (14) [22].

$$\Gamma_L = \frac{Z_L - Z_o}{Z_L + Z_o} \tag{14}$$

In the system, the typical value of the load impedance Z_L is much more than that of the cable Z_o, therefore the reflection factor Γ_L is closely limited to a unity. Be aware that $\Gamma_L = 1$ means the reflected voltage from the RL load-side cable terminal. After another time propagation delay τ, $V_{L1}^-(s)$ reaches the MLFC terminals, another

reflection waves occurs due to the mismatch between the MLFC and the cable impedances. The occurrence voltage $V_{s2}^+(s)$ and its RVW, $V_{s2}^-(s)$ are expressed by (15) and (16).

$$V_{s1}^+2s) = V_{L1}^+(s)e^{-\tau s} \tag{15}$$

$$V_{s2}^-(s) = \Gamma_s V_{s2}^+(s) \tag{16}$$

Where, Γ_s is the constant of the reflection at the inverter side is obtained by (17) [22].

$$\Gamma_s = \frac{Z_s - Z_o}{Z_s + Z_o} \tag{17}$$

Since $Z_o \approx 0$, Γ_s is close to the "-1". Notice that $\Gamma_s = -1$ indicates that the voltage is completely reflected at the inverter terminals. The RWPs continue in the same way until the load terminal voltage is mitigated to the DC-link voltage level V_{dc}. By adding up the incident and RVWs at the load terminals, the load terminal voltage, $V_L(s)$ can be expressed by (18) [22].

$$V_{L(s)} = \frac{U(s)(1+\Gamma_s)e^{-\tau s}}{1 - \Gamma_s \Gamma_L} \tag{18}$$

Figure 5 illustrates the MATLAB simulation results of a voltage waveform, where the time rising is 20 ns.

3.2.3. Rising/falling time impact on the RWP
In the MLFC system, in add-on to the mismatching between the TL and load impedances, the rising and falling time (t_r/t_f) of the output voltage is a different essential reason that influences the overvoltage of the load, where if the $(t_r \ll 3\tau)$, a full RVW will be created; V_L is obtained by 19 [26].

$$V_L = (1 + \Gamma_L)V_{DC} \tag{19}$$

According to in (15) and (20), the maximum load voltage will be doubled compared with the inverter peak-to-peak voltage, i.e., 2DC-link voltage. If $(t_r \gg 3\tau)$, the maximum load voltage can be expressed as in (20) [26].

$$V_L = \left(\frac{3\,\Gamma_L}{v\,t_r} + 1\right)V_{DC} \tag{20}$$

The variation of the standardized maximum load voltage together with the length of the cable and increase in time is illustrated in Figure 6.

3.2.4. MLFC controlled DC-link voltage power port model
As illustrated in Figure 7, the MLFC is controlled according to the IG torque requirement, speed fluctuations, and IG parameters. The DC-link voltage has no significance in terms of operation and control. Moreover, the DC-link power and voltage are not imposed, and hence, they need to be regulated. Therefore, the MLFC is connected to the (RL load) system via a controlled rectifier.

Figure 7 is treated as a black box that exchanges a time-varying power P_{ext} with the MLFC DC-link. Therefore, the MLFC system is called a controlled DC-link voltage power port as it enables the exchange of power in both directions between the DC-link power source and the RL load. Depending on the operational conditions of MLFC, P_{ext} may be positive or negative in both transient and quasi-stationary states [26].

Usually, $P_{ext}(t)$ is an external signal that cannot be controlled by the power electronic converter system. Hence, to avoid any instability or excursions in the power and consequently, in the DC-link voltage, V_{DC}, the regulated power outlet of Figure 7 requires the regulation of V_{DC}. The power balance and regulation are achieved through the use of (21).

$$P_{ext} = i_{ext}\,V_{DC} + \frac{d}{dt}\left(\frac{C_1}{2}\,V_{DC}^2\right) + i_{C1}\,V_{DC} = P_{DC} + \frac{C_1}{2}\,\frac{dV_{DC}^2}{dt} + P_{loss} \tag{21}$$

Where P_{DC} represents the controlled DC power at the DC-link of MLFC that could be represented by the multiplication of the input DC-link current, i_{ext} with the DC-link voltage V_{DC}, and P_{loss} is the time rate of change in the energy loss at the terminals of the effective capacitor at the DC-link of MFLC. In (21) represents the dynamic behavior of the system in which the control input is P_{DC}, and the state variable may be the square value of the DC-link voltage, V_{DC}^2, P_{ext} and P_{loss} represent the disturbance signals acting at the input of the

wind PS. Therefore, it is preferred to regulate the V_{DC}^2 rather than the voltage itself, V_{DC} [26]. Replacing $P_{DC} = P_t$ and after substituting into (21) and rearranging, we get (22).

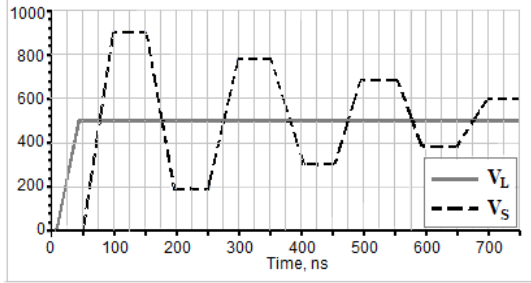$$\frac{1}{2} C_1 \frac{dV_{DC}^2}{dt} = P_{ext} - P_{loss} - P_t \tag{22}$$

Figure 5. Idealized waveforms of the inverter, and RL load voltages under RWP in the MLFC system
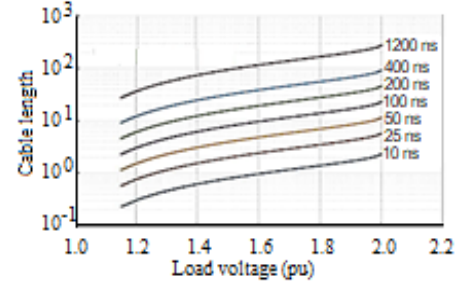

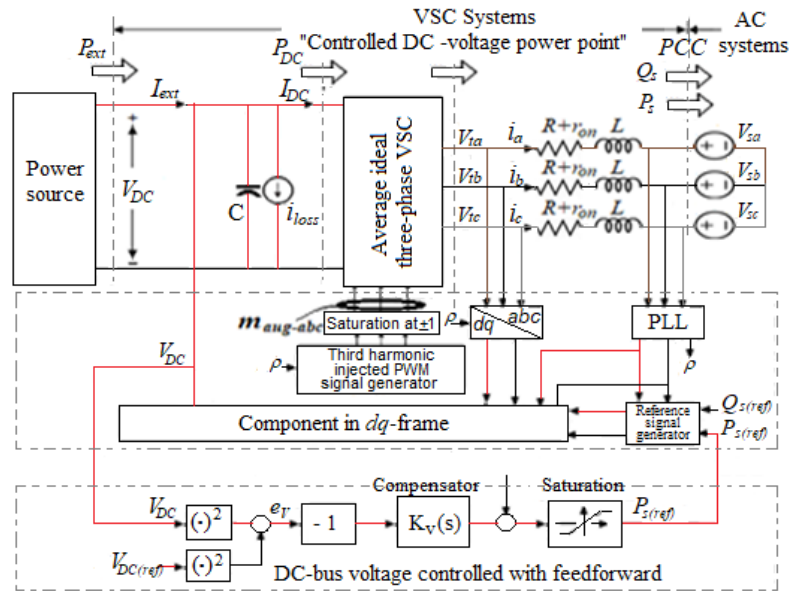Figure 6. The RL load voltages at various cable lengths and rise times

Figure 7. Block diagram of the regulated DC-link voltage power port

Where P_t is the terminal power of the MLFC AC side. V_{DC}^2, P_t, and P_{ext} with P_{loss} are the state variable and output, the control input and disturbance inputs of the dynamic system represented by (22). Hence, to control V_{DC}^2, one can form the block diagram presented in Figure 7, which consists of an internal control loop interlaced inside an outer loop. V_{DC}^2 is compared through the external loop with the reference $V_{DC(ref)}^2$, handles errors with the compensator, and submits $P_{S(ref)}$ to the internal control loop. The internal control loop is the active power control unit that regulates P_S at its reference value $P_{S(ref)}$ as explained in detail in [26]. Hence, P_S and Q_S are controlled through control signals in the dq frame generated from processing the direct and quadrature current components from the AC load system via special compensators.

4.   SIMULATING DFIG-BASED WT WITH RL LOAD AND LONG LENGTH CABLES

In this paper, the DFIG-based wind PS feeding three-phase isolated RL load through a long cable is simulated, analyzed, and studied using Figure 8. The simulation parameters of the IG are given in Table 1. To better understand the above-mentioned TL resonance (long cable) and wave reflections, this is facilitated by using a computer simulation method, as it is necessary to consider both voltage and current waves.

Table 1. Parameters of a DFIG model

Parameters	Symbol	Value	Parameters	Symbol	Value
Stator winding resistance	R_S	26.37mΩ	The number of poles	p	2
Rotor winding resistance	R_r	14.14mΩ	AG nominal frequency	ω_o	377 rad/s
Stator winding inductance	L_S	7.3073mH	Nominal field emf	U_p	30V
Stator winding leakage inductance	$L_{S\sigma}$	0.3676mH	Initial stator angle	α	-1.5708°
Rotor inductance	L_r	7.0571mH	Initial rotor angle	β	-1.5708°
Rotor winding leakage inductance	$L_{r\sigma}$	0.1174mH			

The used switching mode provides control pulses for the voltage source inverter, based on the comparison of three reference modified sine waves, with a triangular reference signal to produce needed gate signals as described in [24]. These three modified sinusoidal reference waves are shifted concerning each other by 120°. The gate control signals are derived from the points of intersection of the sinusoidal and the triangular signals. The provided control signals can be used to control static semiconductor switches. "If the control signal value is > 0", the main switch is turned on. "If the control signal value is <= 0", the main switch is turned off. Instead of maintaining the width of all pulses, the width of each pulse varies proportionally to the rated modified sine wave amplitude at the center of the same pulse.
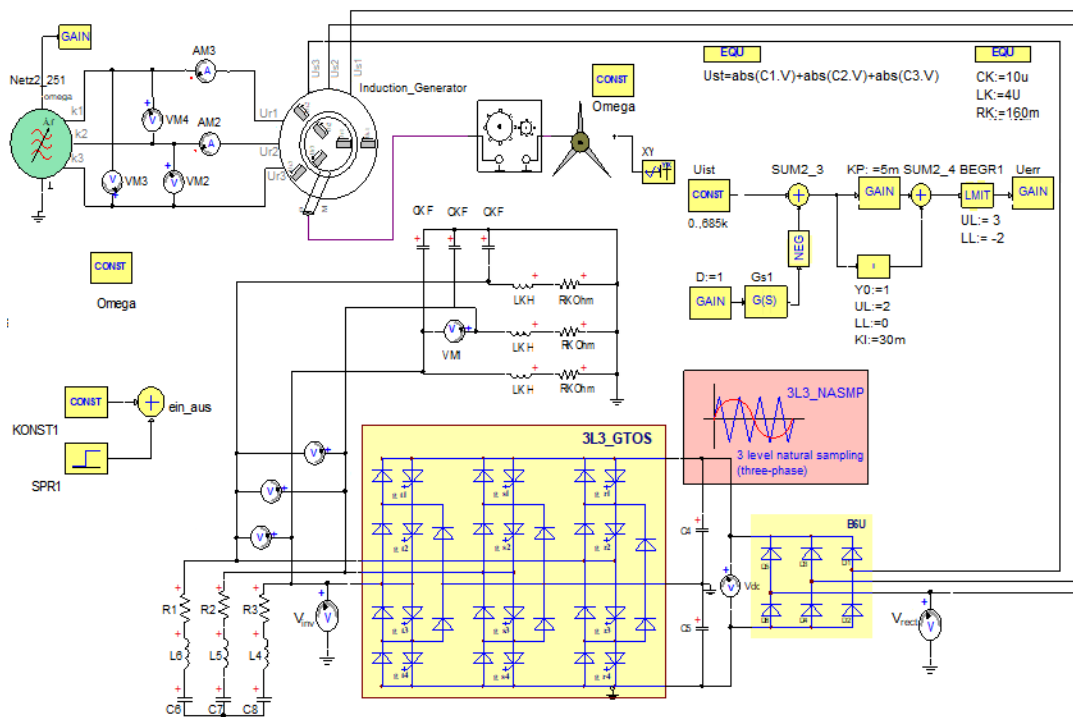

Figure 8. Simulation structure of the DFIG-based VSWT feeding RL load through long cable

The WT driving the DFIG has the following parameters: the turbine IG of inertia is about 2×10^4 kg. m²; the rotor radius R = 35m; the number of blades is 3 and the initial WS and position of the turbine rotor at zero value. WS is imposed and kept constant at 10m/s. The terminal on the "AC" side of each half of the MLFC bridge is connected to one phase of the RL load through a long cable. Thus, the RL load is interfaced with the inductors of the cable through three "$R_{TL} = 0.1\Omega$" resistors, in series with an inductor of "$L_{TL} = 100\ \mu H$". The load resistance is "$R_L = 0.5\Omega$", and an inductance "$L_L = 1mH$". The three-level frequency with a capacitive voltage divider allows a bi-directional flow of power from the "DC" side to the load. The capacitance of each capacitor on the DC-link $C_4 = C_5 = 5\mu F$.

Figure 9(a) shows, respectively, the voltage and current waveforms of the DFIG with their direct and quadrature components. The amplitudes of the terminal line voltages of DFIG are invariable after $t = 0.5\ s$. The motive is that the direct component and the quadrature component of the rotor voltage of the DFIG are also invariable through the previous time interval. But the amplitude of the torque rises with ω. This is expected due to the relation of $V_{S(d)}$ with $V_{S(q)}$ on ω. Figure 9(b) illustrates the phase current waveform of the load and

DC-link voltage of Figure 8 when the compensation is not enabled in the DC-link voltage control loop. Moreover, initially, the controllers are inactive, and the MLFC gating pulses are produced as explained above.
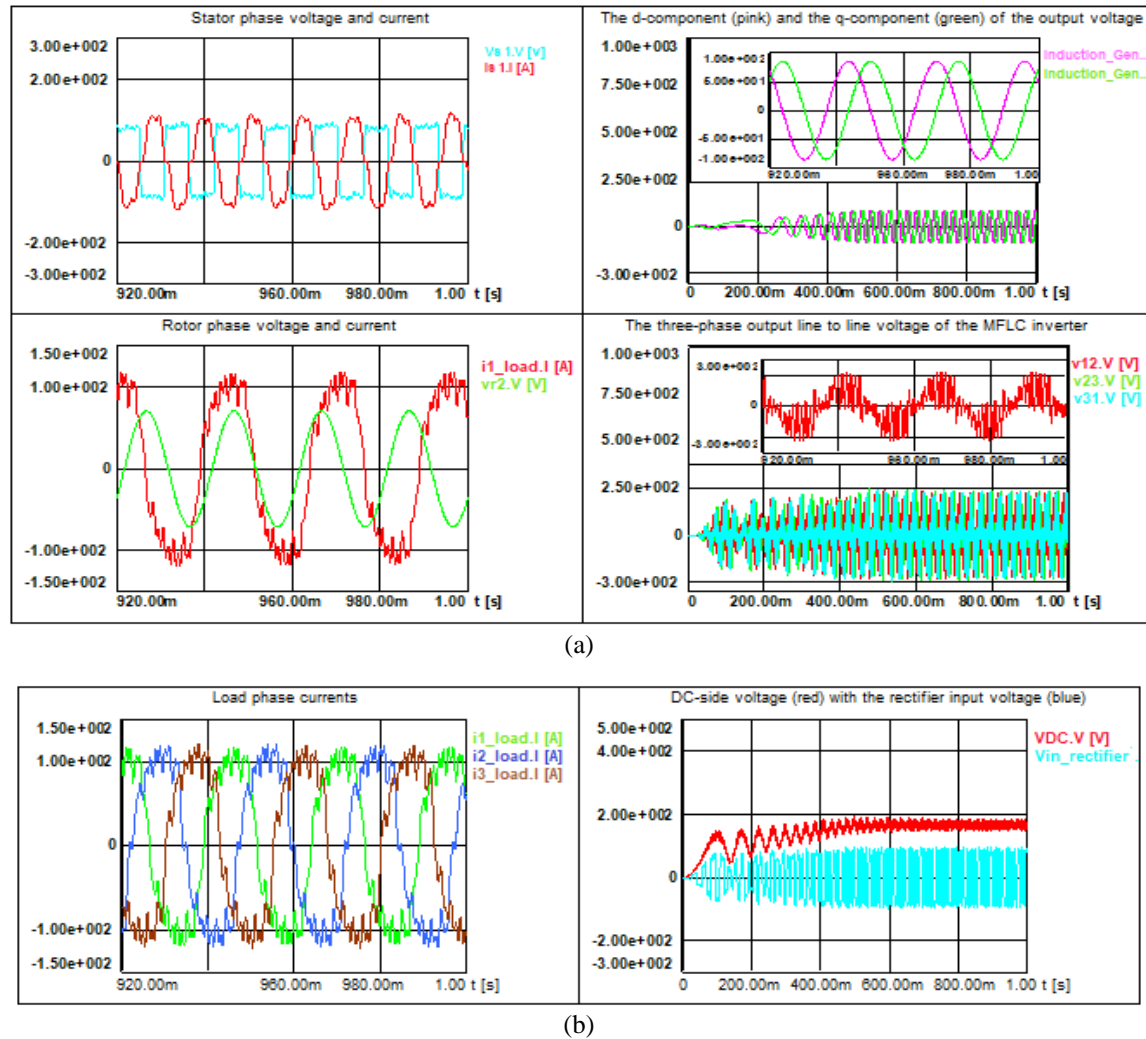

(a)

(b)

Figure 9. Simulation results of the VSWT system (a) waveforms of the generator stator and rotor voltages with MLFC and (b) waveforms of currents and voltages at both sides of MLFC

Thus, the DC-link capacitor (C_4 and C_5) is gradually charged to about 180 V by the MLFC switches units. To restrict the value of the charging current of the DC-link capacitor, and also to cancel large fluctuation of the V_{DC}, a greater value of this capacitor must be chosen. Also, a well-tuned DC-link voltage controller could force P_{DC} to be negative as illustrated in Figure 10. Figure 10 also illustrates that P_s has a small value corresponding to P_{DC}. However, the DC-link voltage controller may increase P_s to maintain a balance of power.

Figure 10(a) shows the dynamic response and voltage-current waveforms of the DFIG-based VSWT. The proposed system in this paper under the effect of using a MLFC instead of a two-level three-phase bridge inverter. A comparison between Figures 9 and 10 shows that the deflections of the actual value of V_{DC} from its average value are considerably smaller in the proposed system with a MLFC. However, the voltage V_{DC} system has a larger average value generated in the system with MLFC as compared to that with the two-level inverter. Also, the difference between the power on the DC-link of the two-level inverter P_{DC}, and the power, P_{out} on its AC side is very large in preference to the P_{DC}. Therefore, the DC-link voltage power port of the MLFC transfers about 6kW to its corresponding AC side in the inverting mode of operation, while it cannot reach more than 4kW of its rated capacity in the inverting mode of operation with the two-level inverter.

Furthermore, as it is mentioned previously in this paper, the TL does not generate any resonance or standing waves of voltages and currents across its corresponding load when it is terminated with an impedance that is almost equal to its characteristic impedance. Otherwise, it is said to be resonant with fast reflections of

current/voltage waves that cause high harmonics to be generated within the load and thereby in the whole system. The illustration indicated in Figure 10b for the three-phase input current of the RL load with the two-level inverter shows how a negatively changing sinusoidal-shaped standing waveform is generated upon reaching the line's end at the load.
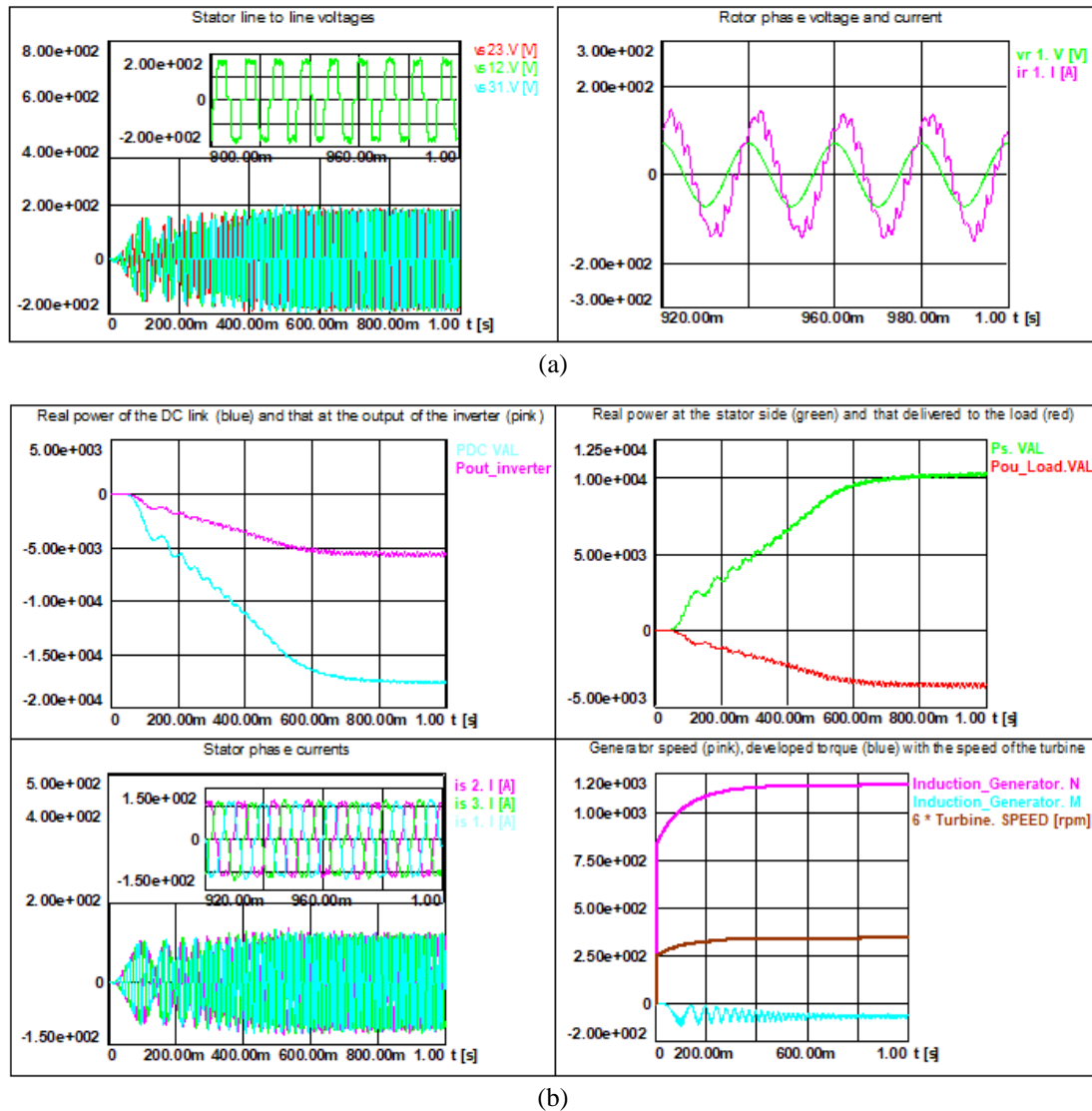

(a)

(b)

Figure 10. Simulation results (a). Voltage and current waveforms of the generator windings and (b) Real power waveform of the DC-link, at the stator side, stator phase current in addition to the dynamic behavior of DFIG and the turbine applied torque with such inverter.

By improving the terminals voltage waveform of the inverter, the present torque ripple in the DFIG is reduced, and its performance efficiency is enhanced. However, one of the modulation/control strategies used in this paper to generate gating signals for the switches of the three-level MLFC is the sinusoidal PWM technique, modified by using a third harmonic injected PWM reference signal. Running this proposed simulation illustrates the reflection of the current waves (standing waves). It was seen that using PWM MLFC instead of the conventional 2`-level inverter could eliminate this phenomenon.

5. CONCLUSION

This study is focused on the design of a control system for a stand-alone DFIG-based VSWT, feeding an RL load through a long cable with the ability to use fast-switching modes. Additionally, the results show

that with the use of a 3-level MLFC, it is possible to achieve a perfect match between the transmission line impedance and the RL load impedance. As a result, no standing waves are generated, and thus no high harmonics in the system. Compared with the traditional PWM inverter.

The simulation results show that the suggested control approach is well-suited to regulating the DFIG-based VSWT system, with control objectives met in both smooth and randomly variable turbulent WS. As a result, this MLFC-based driving system offers benefits such as lower overall harmonic distortion, higher efficiency, lower shunt losses, and a higher output base voltage. Finally, the study looks at how changes in wind and rotor speed affect the frequency of the induced rotor voltage and the active power flow. The variation of the transmission line parameter affects the mismatch between the load impedance and the characteristic impedances of the TL. Such a phenomenon creates standing waves depending on the length of the TL and speed of propagation.

This phenomenon has been studied and verified in Simplorer/MATLAB. The PWM MLFC is recommended, according to the simulation findings since it maintains a constant load frequency and controlled voltage regardless of load variation and/or wind speed. The fixed load frequency is reached by regulating the rotor windings frequency, such that a fixed stator windings frequency is kept fixed at any WT shaft speed. The magnitude of the IG terminal voltage is regulated by adjusting the rotor terminal voltage and, thus, current. The effectiveness of the proposed modulation MLFC has been verified using a simulation model over a wide operating range, including sub and super-synchronous speeds.

REFERENCES

[1]   S. S. Sakthi, R. K. Santhi, N. M. Krishnan, S. Ganesan, and S. Subramanian, "Wind Integrated Thermal Unit Commitment Solution using Grey Wolf Optimizer," *International Journal of Electrical and Computer Engineering (IJECE)*, vol. 7, no. 5, pp. 2309-2320, 2017, doi: 10.11591/ijece.v7i5.pp2309-2320.

[2]   A. Hamzeh, S. A. Hamed, and Z. Al-Omari, "Wind Generation Impact on Symmetrical Fault Level at Grid Buses," International *Journal of Electrical and Computer Engineering (IJECE)*, vol. 8, no. 5, pp. 2682-2690, 20148, doi: 10.11591/ijece.v8i5.pp2682-2690.

[3]   A Hamzeh, and Z Alomari, "Grid Impacts of Full Interface Converter Wind Generation on Balanced Fault Response," *GCREEDER 2013*, Am-man-Jordan, September 10th – 12th, pp. 1-9, 2013.

[4]   A. Hamzeh, S. Hamed, and Z. Al-Omari, "Design and Construction of a Small Stand-Alone Wind Turbine Using Scrap Materials," *Renewable Energy and Sustainable Buildings*, pp. 379-390, 2019, doi: 10.1007/978-3-030-18488-9.

[5]   W. Emar and O. A. Saraereh, "Simulated topology of doubly powered induction motor with diode clamped inverter," *International Journal of Power Electronics*, vol. 10, no. 1-2, pp. 173-185, 2019, doi: 10.1504/IJPELEC.2019.096839.

[6]   S. W. Lee and K. H. C. Lee, "Adaptive Sliding Mode Control for PMSG Wind Turbine Systems," *Energies*, vol. 12, no. 4, pp. 1-17, 2019, doi: 10.3390/en12040595.

[7]   A. B. E. Pant, "Modelling and Design of Grid Connected Doubly Fed Induction Generator," M.S. thesis, Electrical and Computer Engineering, Texas Tech University, pp. 1-82, 2019.

[8]   X. Li, M. Yahui and C. Yijia, "An Equivalent Model of Doubly-Fed Wind Generation System," *Transactions of China Electrotechnical Society*, vol. 30. no. 8, pp. 210-217, 2015.

[9]   Amirnaser Yazdan and Reza Iravani, "Voltage-Sourced Converters In Power Systems: Modeling, Control, And Applications," *John Wiley & Sons, Inc.-IEEE Press*, 2010.

[10] N. Nisso, D. Raïdandi, N. Djongyang and F.D. Menga, "Modeling and analysis of boost converter in small-signals applied to the wind energy conversion system using Matlab/Simulink," *Revue des Energies Renouvelables*, vol. 21, no. 4, pp. 635-649, 2018.

[11] D. W. Hart., "Power electronics," New York: McGraw-Hill, 2011.

[12] Y. C. Chang, C. C. Tsai and Y. L. Lu, "Current Control of the Permanent-Magnet Synchronous Generator Using Interval Type-2 T-S Fuzzy Systems," *Energies*, vol. 12, no. 15, pp. 1-12, 2019, doi: 10.3390/en12152953.

[13] Y. Ma, L. Tao, X. Zhou, W. Li and X. Shi, "Analysis and Control of Wind Power Grid Integration Based on a Permanent Magnet Synchronous Generator Using a Fuzzy Logic System with Linear Extended State Observer," *Energies*, vol. 12, no. 15, pp. 1-19, 2019, doi: 10.3390/en12152862.

[14] M. Fdaili, A. Essadki, M. Nadour and T. Nasser, "Comparative Study of MPPT and Pitch Angle Control Strategies for a Wind Energy Conversion System," *International Renewable and Sustainable Energy Conference (IRSEC)*, 2017, pp. 1-6, doi: 10.1109/IRSEC.2017.8477291.

[15] F. Mazouz, S. Belkacem, I. Colak, S. Drid and Y. Harbouche, "Adaptive direct power control for double fed induction generator used in wind turbine," *International Journal of Electrical Power & Energy Systems*, vol. 114, pp. 1-11, 2020, doi: 10.1016/j.ijepes.2019.105395.

[16] A. Dali; S. Abdelmalek; A. Bakdi and M. Bettayeb; "A new robust control scheme: Application for MPP tracking of a PMSG-based variable-speed wind turbine," *Renewable Energy*, vol. 172, pp. 1021-1034, 2021, doi: 10.1016/j.renene.2021.03.083.

[17] J. Talla, V. Q. Leu, V. Šmídl and Z. Peroutka, "Adaptive Speed Control of Induction Motor Drive With Inaccurate Model," *IEEE Transactions on Industrial Electronics*, vol. 65, no. 11, pp. 8532-8542, 2018, doi: 10.1109/TIE.2018.2811362.

[18] Cheng Zhang, Franck Plestan, "Adaptive sliding mode control of floating offshore wind turbine equipped by permanent magnet synchronous generator," *Wind Energy*, vol. 24, pp. 754–769, 2021.

[19] M. P. Kazmierkowski, R. Krishnan, and F. Blaabjerg, "Control in Power Electronics," *Selected Problems, Academic Press, 1st Edition, Elsevier Science* (USA), 2002.

[20] W. Zhou, M. S. Diab and X. Yuan, "Impact of Parasitics and Load Current on the Switching Transient Time and Motor Terminal Overvoltage in SiC-Based Drives," *IEEE Energy Conversion Congress and Exposition (ECCE)*, 2020, pp. 225-232, doi: 10.1109/ECCE44975.2020.9235417.

[21] B. Narayanasamy, A. S. Sathyanarayanan, F. Luo and C. Chen, "Reflected Wave Phenomenon in SiC Motor Drives: Consequences, Boundaries, and Mitigation," *IEEE Transactions on Power Electronics*, vol. 35, no. 10, pp. 10629-10642, 2020, doi: 10.1109/TPEL.2020.2975217.

[22] M. S. Diab and X. Yuan, "A Quasi-Three-Level PWM Scheme to Combat Motor Overvoltage in SiC-Based Single-Phase Drives," *IEEE Transactions on Power Electronics*, vol. 35, no. 12, pp. 12639-12645, 2020, doi: 10.1109/TPEL.2020.2994289.

[23] R. Ruffo, P. Guglielmi and E. Armando, "Inverter Side RL Filter Precise Design for Motor Overvoltage Mitigation in SiC-Based Drives," *IEEE Transactions on Industrial Electronics*, vol. 67, no. 2, pp. 863-873, 2020, doi: 10.1109/TIE.2019.2898623.

[24] S. Lee and K. Nam, "An overvoltage suppression scheme for AC motor drives using a half DC-link voltage level at each PWM transition," *IEEE Transactions on Industrial Electronics*, vol. 49, no. 3, pp. 549-557, 2002, doi: 10.1109/TIE.2002.1005379.

[25] W. Zhou, M. S. Diab and X. Yuan, "Mitigation of Motor Overvoltage in SiC-Device-Based Drives using a Soft-Switching Inverter," *IEEE Energy Conversion Congress and Exposition (ECCE)*, 2020, pp. 662-669, doi: 10.1109/ECCE44975.2020.9236099.

[26] W. Emar, Z. Huneiti, and Z. Al-Omari, "Induction motor current ripple minimization with PV based SEPIC-cascaded inverter," *International Journal of Modelling, Identification, and Control*, vol. 35, no. 2, pp. 151-165, 2020.

BIOGRAPHIES OF AUTHORS

Zakaria Al-Omari 🔟 🔗 SC Ⓟ was born in Irbid Jordan on June 3, 1966. He obtained his Ph.D. degree from the Faculty of Energy, Vinnytsia National Technical University, Ukraine in 1998. Currently, he is an Associate Professor in the Renewable Energy Engineering Department at the Faculty of Engineering, Isra University in Amman, Jordan. His main interests are minimizing power system losses, renewable energy, load forecasting, reliability, and efficiency. He has published 16 technical papers in Journals and international conferences. He can be contacted by email: zakaria.alomari@iu.edu.jo.

Walid Emar 🔟 🔗 SC Ⓟ received his Ph.D. degree in power electronics and control in 2002 from the University of West Bohemia, Czech Republic. He worked for different institutes in his field in the Czech rep. such as Škoda Company, Japanese air-conditioning Daikin, and Fuji Koyo. Currently, He is at Isra University, Jordan as a full-time professor teaching Energy Management for master's degree students and control systems, in addition to power electronics and other subjects for undergraduate students. He is also engaged in research in renewable energy systems, energy management, electrical engineering for renewable and sustainable energy systems, control of power electronics, and control. He can be contacted at email: walid.emar@iu.edu.jo